IOP Publishing Phys. Med. Biol. 65 (2020) 035004 (15pp) https://doi.org/10.1088/1361-6560/ab623f

Physics in Medicine & Biology

IPEM Institute of Physics and Engineering in Medicine

PAPER

The impact of sensitive volume thickness for silicon on insulator microdosimeters in hadron therapy

D Bolst[1], S Guatelli, L T Tran and A B Rosenfeld

Centre for Medical Radiation Physics, University of Wollongong, Wollongong, Australia

[1] Author to whom any correspondence should be addressed.

E-mail: db001@uowmail.edu.au

RECEIVED
3 September 2019

REVISED
25 November 2019

ACCEPTED FOR PUBLICATION
16 December 2019

PUBLISHED
24 January 2020

Keywords: microdosimetry, hadron therapy, silicon-on-insulator (SOI), sensitive volume dimensions, Geant4

Abstract

Compact silicon on insulator (SOI) microdosimeters have been used to characterise the radiation field of many different hadron therapy beams. SOI devices are particularly attractive in hadron therapy fields due to their spatial resolution being well suited to the sharp dose gradients at the end of the primary beam's range. Due to the small size of SOI's sensitive volumes (SVs), which are usually ~1–10 μm thick, the fabrication of these devices can present challenges which are not as common for more conventional thickness silicon devices such as silicon spectroscopy detectors. Microdosimetry is the study of the energy deposition in micrometre sized volumes representing biological sites and is a powerful approach to estimate the biological effect of radiation on the micron-scale level, in a cell. However, cell sizes vary extensively translating in different energy deposition spectra. This work studies SV thicknesses between 1 and 100 μm using Geant4 and examines the impact of SV dimensions on microdosimetric quantities. The quantities studied were the frequency mean lineal energy, $\overline{y_F}$, and the dose mean lineal energy, $\overline{y_D}$. Additionally the relative biological effectiveness (RBE), estimated by the microdosimetric kinetic model (MKM), is also investigated. To study the impact of the SV thickness, SOI microdosimeters were irradiated with proton, ^{4}He and ^{12}C ion beams with ranges of ~160 mm, with the microdosimeter being set at various positions along the Bragg curve. It was found that $\overline{y_F}$ was influenced the least in proton beams and increased for heavier ion beams. Conversely, $\overline{y_D}$ was impacted by the SV thickness the most in proton beams and ^{12}C was the least. Similar to $\overline{y_D}$, protons were impacted the most by the SV thickness when estimating the RBE using the MKM. The cause of these differences was largely due to the different densities of the delta electron track structure for the case of $\overline{y_F}$ and the energy transferred to the medium from the primary beam for $\overline{y_D}$.

1. Introduction

Microdosimetry is the method of measuring the energy deposition from radiation in micron-sized sensitive volumes (SVs), representing the dimensions of biologically sensitive sites in cells (Rossi and Zaider 1996). At this scale the stochastic nature of energy loss due to the fluctuations in the number of ionisations/excitations in the medium and the amount of energy transferred in each of these events becomes significant (ICRU Report 36-Microdosimetry 1983, Kellerer 1985). Microdosimetry is a particularly powerful method for estimating the radiobiological effect of a radiation field, regardless if it is a single particle source or a complicated mixed radiation field. The radiation field produced in hadron therapy is particularly complex due to the various inelastic hadronic interactions (Schardt *et al* 2010), making microdosimetry particularly well suited for characterising the radiation field for both in-field (Tran *et al* 2018) and out-of-field (Chartier *et al* 2017).

Microdosimetry measurements are traditionally performed using tissue equivalent proportional counters (TEPCs). The physical SVs of commercial TEPCs are commonly of the order of 10 mm in diameter and are filled with a tissue equivalent gas which is often methane or propane based (Far 2001). More compact TEPCs are also produced for research purposes such as mini-TEPC designs (Kliauga 1990, De Nardo *et al* 2004, Selva *et al* 2017) which use considerably smaller gas chambers, often cylindrical in shape. The relatively large volume of TEPCs are

capable of making measurements which represent the sizes of cells by using a low gas pressure. Traditional commercial TEPCs have a number of limitations, one is its large size, which makes measurements of the Bragg peak (BP) at the end of an ion's track, which have sharp dose gradients, to be smeared out. Furthermore, the operation of the TEPC requires a high voltage supply, of the order of several hundred volts and a complex gas supply, meaning portability and setup can be challenging. An alternative to the general TEPC design is to instead adopt solid state designs, such as silicon on insulator (SOI), which allow for simpler and more compact designs which have operating voltages of ∼10 V (Rosenfeld 2016).

Conceptually, microdosimeters are used to represent the dimensions of sensitive sites in biological cells and estimate the biological response from radiation. Regardless of whether these sites are represented by a TEPC or a silicon SV, the choice of what size site is the 'best' to be represented is not a clear choice. Commonly, when commercial TEPCs are used for microdosimetric measurements, a simulated tissue equivalent diameter between ∼0.5 and 10 μm is used, while the thickness of the silicon SVs in SOI devices are often ∼1–10 μm. The cell nucleus is of major importance when considering radiation damage since it contains the cell's DNA. Sufficient damage to the DNA will cause the cell to die (Nikjoo *et al* 2016). Due to the importance of the nucleus for cell survival and replication, the energy deposition in a cell nucleus sized volume is more relevant than a whole cell when studying the radiation damage to a cell, which is largely the assumption made when using microdosimeters. There are over 200 different cell types in the human body, however, the size of most cell nuclei have a fairly narrow range, with most nuclei diameters ranging from 2 to 10 μm (Milo and Phillips 2015). HeLa cells are commonly used in cancer research (Masters 2002) and have an average cell nucleus volume of ∼690 μm^3 (Milo and Phillips 2015, Maul and Deaven 1977), which if contained as a perfect sphere corresponds to a diameter of ∼11 μm. For some biological models, such as the microdosimetric kinetic model (MKM), the 'sensitive' site of interest are sub-nuclei volumes referred as 'domains' in the MKM. Human salivary gland (HSG) tumour cells are commonly used as a reference cell for predictions and have domain sizes of ∼0.8 μm in diameter (Kase *et al* 2006).

Because of the range of cell nuclei, it is valuable to know how a microdosimetric measurement will be affected based upon the simulated size of the detector's SV. Appendix F of the (ICRU Report 36-Microdosimetry 1983) has compiled many studies which have investigated the effect of varying the simulated size of a SV in a TEPC on microdosimetric measurements. Such studies have mainly used the radiation field of photon and electron sources, with fewer focused on neutrons and low energy protons and α particles. Very few investigations have reported the impact of changing the simulated volume size on the microdosimetric measurements in therapeutic hadron beams using microdosimeters. Due to the logistics and cost of creating a silicon microdosimeter design with many different SV thicknesses, microdosimetric studies comparing different SV sizes of SOI devices is sparser than TEPCs.

This work examines the impact on microdosimetric quantities as well as the RBE, estimated using the modified MKM (Kase *et al* 2006), for SOI designs with silicon thicknesses from 1 to 100 μm when placed in proton, ^{4}He and ^{12}C ion beams of therapeutic energies. To investigate this impact Monte Carlo simulations were performed using the Geant4 toolkit (Agostinelli *et al* 2003, Allison *et al* 2006, 2016).

2. Materials and methods

2.1. Simulation setup

Geant4 (version 10.2p3) was adopted to study the impact of varying the SV size of SOI microdosimeters on microdosimetric quantities. The SV thicknesses investigated were: 1, 2.5, 5, 10, 25, 50 and 100 μm. Based on previous studies, the diameter of the cylinder is set to be twice its height (thickness), this geometry corresponds to the mean chord length being the same as the thickness, causing radiation with an angular distribution closely representing an isotropic distribution (such as delta electrons) to traverse the detector with a mean chord length equal to the thickness (Bolst *et al* 2018), discussed more below in section 2.2. The different microdosimeters were placed in a 30 × 30 × 30 cm^3 water phantom and was irradiated in mono-energetic: proton, ^{4}He and ^{12}C ion beams with initial energies of 150, 150 and 290 MeV/u, respectively. Each beam was generated with 40 cm of air between their starting position and the water phantom, as shown in figure 1(a). Each beam was generated with a Gaussian distribution of 11 mm σ with no angular divergence and an energy σ of 1%, 0.35% and 0.2% for the proton, ^{4}He and ^{12}C beams, respectively. The response of the microdosimeter was investigated along the central axis of the different beams (in-field configuration).

The SOI microdosimeter design used in this study was based on a three dimensional 'mushroom' design, which is made of arrays of cylindrical SVs embedded in PMMA and supported on a 1 μm thick silicon oxide layer. This design has been previously studied in Bolst *et al* (2017b) in a ^{12}C ion beam and later optimised in Bolst *et al* (2018) in proton and ^{12}C ion beams. The design of the microdosimeter is shown in figure 1(b), which shows a side view and a beam's eye view of two different thick SV designs. In this study the SVs cover an area of 5 × 5 mm^2

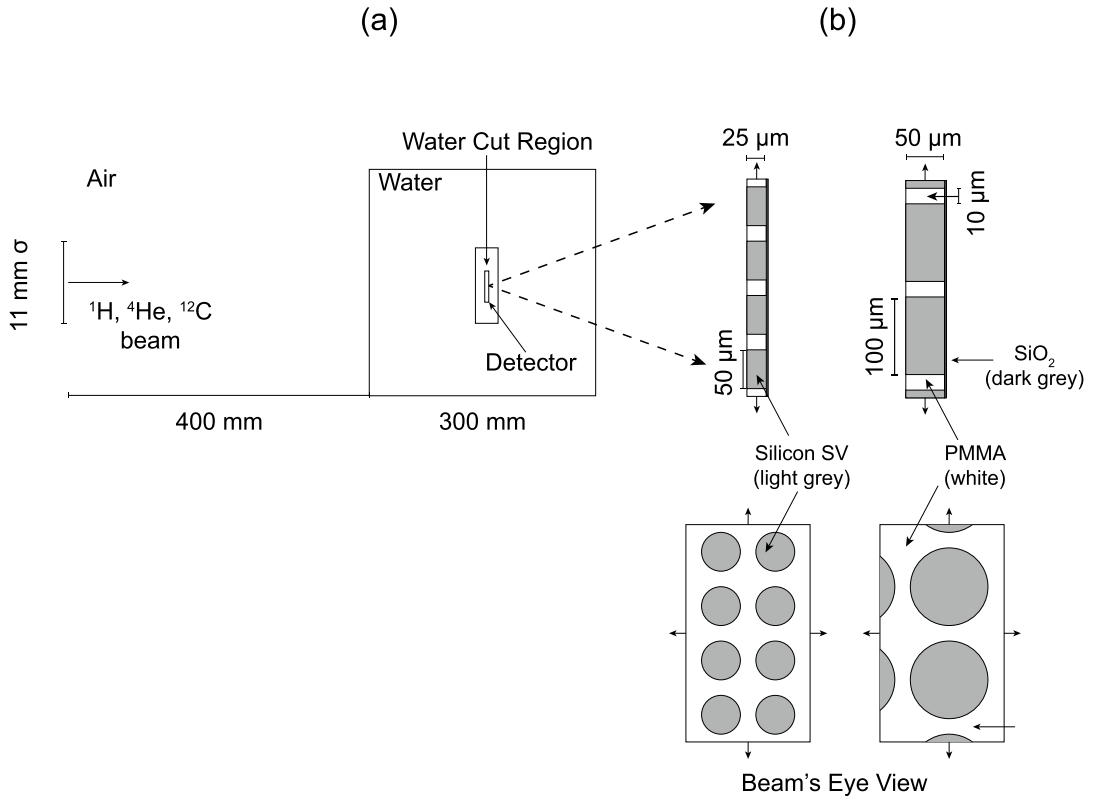

Figure 1. (a) Simulation setup used in this study, showing the generation of the beam incident upon the water phantom which contains a separate water region with a different particle production threshold which houses the microdosimeter detector inside. (b) Shows a zoomed in region of two different sized microdosimeters with the 25 μm thick design on the left and 50 μm design on the right, respectively. The bottom of (b) shows the beam's eye view of the two different sized microdosimeters.

with a distance of 10 μm between the edges of the SVs, as shown in figure 1(b). To mimic the real-world device, the hits in the SVs are processed as if they were connected as a single channel.

The detector was placed in the water phantom with respect to the left side of the SV of the detector (as depicted in figure 1), for example placing the detector at a depth of 100 mm would correspond to the beam traversing 100 mm of water before entering the silicon SV. The pinnacle of the BP, for both the proton and ^{4}He ion beam, occurs at 155 mm, while the ^{12}C ion beam occurs slightly deeper at 162.4 mm. For the proton and ^{4}He ion beams the detectors were placed at depths of: 10, 50, 80, 120, 140, 150, 155 and 160 mm, with the last depth corresponding to the distal edge of the BP. For the ^{12}C ion beam the detectors were placed at: 10, 50, 100, 130, 140, 150, 160, 163.5 and 170 mm. The last depth of 170 mm corresponds to downstream of the BP where all the primary ^{12}C ions have stopped and the quantities calculated at this position are due to secondary particles only. The lineal energy spectra are divided into 4096 equally spaced bins for each beam, with a minimum lineal energy of 0 keVμm. The maximum lineal energy instead had values of 500, 800 and 1200 keV μm^{-1} for the proton, ^{4}He and ^{12}C ion beams, respectively.

When a volume is placed in a radiation field the particles will enter and exit the volume at various angles, creating certain distributions depending on the volume shape and radiation field. Figure 2 shows three chord/path length distributions of three configurations. The distribution labelled as *Gaussian* is a typical distribution which a primary hadron therapy beam would produce when incident upon an SOI microdosimeter 10 μm thick in the direction of the beam. The other two distributions represent the theoretical chord distributions of a sphere in any field, due to it being angularly independent, and a cube when placed in an isotropic field. The diameter of the sphere and the edge of the cube are both 15 μm and correspond to a mean chord length value of 10 μm (which can be calculated using equation (2), discussed below), the same as the Gaussian distribution. Despite all distributions having a mean value of 10 μm, their shapes differ significantly. To see if the different chord/path length distributions of the volumes have an impact on microdosimetric quantities, silicon spheres of varying diameters (thickness) were also simulated. This was done by replacing the cylinder volumes with spheres, with thickness/diameters of 1, 1.5, 10, 15, 100 and 150 μm being simulated. The 1.5, 15 and 150 μm diameter volumes have mean chord lengths of 1, 10 and 100 μm, respectively.

In order to improve the speed of the simulation, the microdosimeter was placed in a water region with a separate energy production threshold, or *cut*, compared to the larger water phantom which this region was placed in,

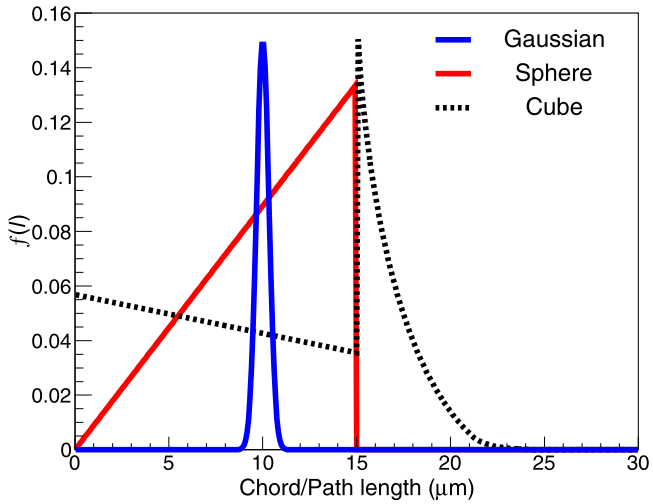

Figure 2. Comparison of different path/chord length distributions for different configurations SVs. The 'Sphere' and 'Cube' distributions are theoretical chord length distributions, the formulas for the theoretical chord length distributions can be found in chapter 3 of Bradley and Rosenfeld (1998).

as shown in figure 1(a). Using the *G4Region* and *G4ProductionCuts* classes, different production thresholds for electrons can be set inside the water region. By choosing a suitable production threshold means that electrons are only generated close to the microdosimeter in the water region. The region has a thickness twice the maximum range of electrons generated by the incident beams plus the thickness of the detector itself. The minimum range of electrons outside of the water region required in order to be generated is set to 1 mm and 2.8 mm for the proton/^{4}He and ^{12}C ion incident beams, respectively, while inside the water region the minimum range of electrons required to be generated was 0.1 μm.

To describe electromagnetic interactions the Livermore physics list was adopted with a production threshold of electrons set to 250 eV. The validity of the electromagnetic models available in Geant4, has recently been documented in the G4Med report (Arce *et al* 2020). The Livermore physics list was shown to agree within 3% of reference data for electron stopping power, which is within the uncertainty limits of the data. The range of protons and ^{12}C ions in water was also reported and Livermore gave agreement within 0.1% for protons and 1.1% for ^{12}C ions compared to experimental measurements. For elastic and inelastic hadron interactions the *G4HadronElasticPhysicsHP* and *G4HadronPhysicsQGSP_BIC_HP* were adopted, respectively. The *G4IonBinaryCascadePhysics* was used to describe hadronic interactions of ions, this model was recently validated against experimental measurements of fragmentation (Bolst *et al* 2017a). For neutron interactions up to 20 MeV the neutron high precision (HP) model was used.

The accuracy of Geant4 for simulating silicon microdosimeters has been performed in proton and heavy ion therapy (HIT) beams. With comparisons performed for both passive (Debrot *et al* 2018) and scanning (Tran *et al* 2017) proton beams. For HIT, ^{12}C, and ion beams in have been compared (Bolst *et al* 2019). For all these previous studies, the silicon microdosimeter investigated had a thickness of ~10 μm. Generally, the simulations and experiment were found to agree within ~10% for the dose mean lineal energy and the relative biological effectiveness, as estimated by the MKM, to be within ~2%. As such, the expected accuracy in the results presented in this study is within ~10%, in terms of the accuracy of the physics models used.

2.2. Microdosimetric quantities under study

In order to study the impact of the SV thickness, the lineal energy spectrum and the microdosimetric quantities of frequency mean lineal energy, $\overline{y_F}$, and the dose mean lineal energy, $\overline{y_D}$, were compared for the different thicknesses. In addition to $\overline{y_F}$ and $\overline{y_D}$, the relative biological effectiveness, RBE, estimated using the modified MKM was also used for comparison.

The lineal energy distributions produced by different sized SVs were compared by using the peak on the right side of the spectrum, produced by the primary beam. The lineal energy peak was compared in terms of its width (full width at half maximum) and its peak position. These quantities were obtained by fitting each lineal energy spectrum (beam type, depth and SV size) data points to a three term Gaussian distribution.

The microdosimetric quantities listed above were calculated using the probability distribution of lineal energy, $f(y)$. The lineal energy, y, is defined as the energy deposited in the SV, ϵ, divided by the mean chord length, $\langle l \rangle$, as shown in equation (1). Where $\langle l \rangle$ is calculated using the Cauchy formula shown in equation (2), where V and S are the volume and surface area of the solid calculating $\langle l \rangle$ for. However, equation (2) only applies for isotropic fields, due to the strong directionality of the radiation field in hadron therapy the $\langle l \rangle$ has been shown to be

inappropriate when the SV is not a sphere, with the mean path length, $\langle l_{Path} \rangle$, being more appropriate (Bolst *et al* 2017b).

$$y = \frac{\epsilon}{\langle l \rangle}, \tag{1}$$

$$\langle l_{\text{Cauchy}} \rangle = \frac{4V}{S}. \tag{2}$$

The $\langle l \rangle$, which calculates the mean of the random distribution of chords within a volume (Kellerer 1984), differs from the $\langle l_{Path} \rangle$, $\langle l_{Path} \rangle$ calculates the mean path length of charged particles traversing the SV using Monte Carlo simulations. Due to the dominance of the primary beam in the energy deposition in hadron beams, the $\langle l_{Path} \rangle$ of just the primary beam is used to calculate the lineal energy. However, if the proportion of primary ions compared to secondary ions falls below 5% then the $\langle l_{Path} \rangle$ of the secondary ions is used to calculate the lineal energy. Due to the thicker SVs investigated in this work compared to previous studies of the $\langle l_{Path} \rangle$ (Bolst *et al* 2017b, 2018), the $\langle l_{Path} \rangle$ is calculated slightly differently. Instead of replacing the silicon SV with a vacuum, the path length is calculated in the silicon volume itself, this is done since the discrepancy between these two quantities may significantly increase towards the end of the beam's range.

Since the measurements are performed in silicon, to obtain a biological relevant spectrum the silicon spectrum must be converted. This involves using a single conversion factor, κ, which scales the silicon spectrum to be tissue equivalent (striated muscle in this case). The conversion factors have previously been found to be 0.58 and 0.57 for proton and ^{12}C beams (Bolst *et al* 2017b), respectively, with 0.58 being adopted for ^{4}He beams here. The proton conversion factor was adopted for ^{4}He due to it being closer to proton than ^{12}C in terms of both charge and mass, with the difference between the proton and ^{12}C conversion factor differing by less than 2%. These conversion factors are based on comparing the spectra of different sized volumes of silicon and tissue equivalent material at different positions along the Bragg curve. The volumes of silicon and tissue equivalent material which produce the most similar energy deposition distribution are then used to calculate the conversion factor from the ratio of their volume size. Due to the ratio of stopping powers not being constant over the therapeutic energy range for tissue equivalent materials and silicon there is an uncertainty of up to 1% associated with these conversion factors.

The final lineal energy for the silicon microdosimeter is calculated using equations (3) instead of (1). Where the κ factor converts the silicon energy deposition spectrum into a tissue equivalent material and $\langle l_{Path,\text{Si}} \rangle$ is the mean path length in the SV calculated using Monte Carlo instead of the mean chord length calculated using Cauchy's formula. These conversion factors show that a thickness of striated muscle is equivalent to ~0.58 of the same thickness of silicon, for example the energy deposition in a 10 μm thick silicon SV is equivalent to 17.3 μm of striated muscle.

$$y = \frac{\kappa\epsilon}{\langle l_{Path,\text{Si}} \rangle}. \tag{3}$$

Once the lineal energy frequency distribution, $f(y)$, is calculated from the energy deposition in the microdosimeter $\overline{y_F}$ and $\overline{y_D}$ can then be calculated. $\overline{y_F}$ is the first moment of $f(y)$ and $\overline{y_D}$ is the ratio of the second and first moment of $f(y)$ which is shown in equations (4) and (5), respectively, where y is calculated using equation (3).

$$\overline{y_F} = \int y f(y) dy \tag{4}$$

$$\overline{y_D} = \frac{\int y^2 f(y) dy}{\int y f(y) dy}. \tag{5}$$

The estimated values of RBE were calculated using the modified MKM, using a 10% cell survival as the biological endpoint. The MKM was first formulated by Hawkins (1994) and was an extension of the theory of dual radiation action (TDRA), which was formulated in the 1970's by Rossi and Kellerer in order to explain the observation that the RBE of neutrons between 100 keV and a few MeV was dependent upon the absorbed dose (Rossi 1970). The MKM was extended by Kase *et al* (2006) for the model to be used in high LET radiation by accounting for *over-killing*, this form of the MKM is referred to as the modified MKM. The basic premise of the MKM considers that cell nuclei are made up of sub-nuclear spherical volumes called 'domains', the 'size' of these domains are cell specific. If a particle track traverses a cell, due to the stochastic nature of energy deposition, there will be a distribution in the amount of energy deposited in the domain volumes. It is then assumed that the probability that a domain survives, S, after some dose, G_d, follows the same form as for low-LET radiation, namely the linear quadratic model (Jones *et al* 2001), as shown in the following. Where A and B are cell specific parameters.

$$S = \exp\left(-AG_d - BG_d^2\right). \tag{6}$$

Following this assumption, the RBE of a radiation source may be estimated based on its dose distribution in the domains.

The modified MKM uses the saturation-corrected dose mean lineal energy term, $y*$, and is defined in equation (7). $y*$ is similar to $\overline{y_D}$ but incorporates over-killing effects at high lineal energies, which is reflected by the saturation parameter, y_0, and has a value of 150 keV μm^{-1}. Over-killing occurs at high-lineal energies where the electron track structure of the ion is so dense that it results in more lethal hits than needed to kill a cell, resulting in 'wasted' dose. Over-killing is important to consider when calculating the RBE since it depends on comparing the doses from different radiation sources to achieve the same biological effect. In this work the HSG cell is used as the reference cell which the MKM is estimating the response of. For HSG cells, events in the SV with a lineal energy greater than 150 keV μm^{-1} was determined to be where over-killing began (Kase *et al* 2006).

$$y^* = y_0^2 \frac{\int (1 - \exp(-y^2/y_0^2)) f(y) dy}{\int y f(y) dy}. \tag{7}$$

Once $y*$ is calculated the α parameter is then calculated using equation (8). The α_0, β, ρ and r_d are specific to the cell line being used as the reference, in this case HSG, which haves values of 0.13 Gy^{-1}, 0.05 Gy^{-2}, 1.0 g cm^{-3} and 0.42 μm, respectively (Kase *et al* 2006).

$$\alpha = \alpha_0 + y^* \frac{\beta}{\rho \pi r_d^2}. \tag{8}$$

Once α is calculated the estimated RBE can then be calculated. Depending on whether the beam is a proton or a heavier ion, the RBE is calculated slightly differently. For HIT beams (larger than protons), the RBE is calculated using equation (9), where $D_{10,x\text{-}ray}$ is the required dose by 200 kVp x-rays to obtain 10% cell survival and has a value of 5 Gy for HSG cells.

$$\mathrm{RBE}_{10} = \frac{2\beta D_{10,x\text{-}ray}}{\sqrt{\alpha^2 - 4\beta \ln(0.1)} - \alpha}. \tag{9}$$

However, for protons, because of their stronger dose dependence for cell survival compared to ions (Jones and Dale 2000), equation (10) is adopted, where the subscript of D is used to reflect the dose dependence. The α_X term is cell specific and has a value of 0.164 Gy^{-1} for HSG cells (Kase *et al* 2013) and D_p is the physical dose delivered to the cell from the proton beam. In this study D_p is the value along the Bragg curve when 1.82 Gy is delivered at the pinnacle of the BP (based on a standard 2 Gy fraction divided by 1.1, using current clinical practice of an RBE of 1.1 in proton therapy (ICRU Report 78-Prescribing, Recording, and Reporting Proton-Beam Therapy 2007)). For recent examples of the modified MKM used in proton therapy fields using silicon microdosimeters see Tran *et al* (2017) and Debrot *et al* (2018), similarly for HIT fields the work of Tran *et al* (2018).

$$\mathrm{RBE}_D = \frac{2\beta D_p}{\sqrt{\alpha_X^2 + 4\beta\left(\alpha D_p + \beta D_p^2\right)} - \alpha_X}. \tag{10}$$

When RBE results are presented and discussed in this work for proton beams the values have been calculated using equation (10) (RBE_D) and for beams larger than protons the values are calculated using equation (9) (RBE_{10}). However, when discussing RBE_D and RBE_{10} both are referred to as RBE for simplicity.

To compare the difference in the above quantities for different SV thicknesses the percentage difference, PD, is used as defined in equation (11). SV_t is the quantity calculated for a sensitive volume with a thickness t and SV_{10} is the quantity for a SV with a thickness of 10 μm.

$$\mathrm{PD} = \frac{\mathrm{SV}_t - \mathrm{SV}_{10}}{\mathrm{SV}_{10}} 100\%. \tag{11}$$

The error bars plotted for $\overline{y_F}$, $\overline{y_D}$ and RBE are calculated by splitting the total number of counts recorded in the detector into ten groups and taking the standard deviation using the 10 sets of counts. The error bars are plotted using a 68% confidence limit.

3. Results

3.1. Impact on the microdosimetric spectrum

The lineal energy spectra ($f(y)$) for the three different beams are shown in figure 3 at a depth of 10 mm (surface of the phantom) and 140 mm (~20 mm before pinnacle of BP). The plots are normalised by scaling the maximum of the primary beam peak (the right most peak in the spectra) to one. An important feature is that the spectra

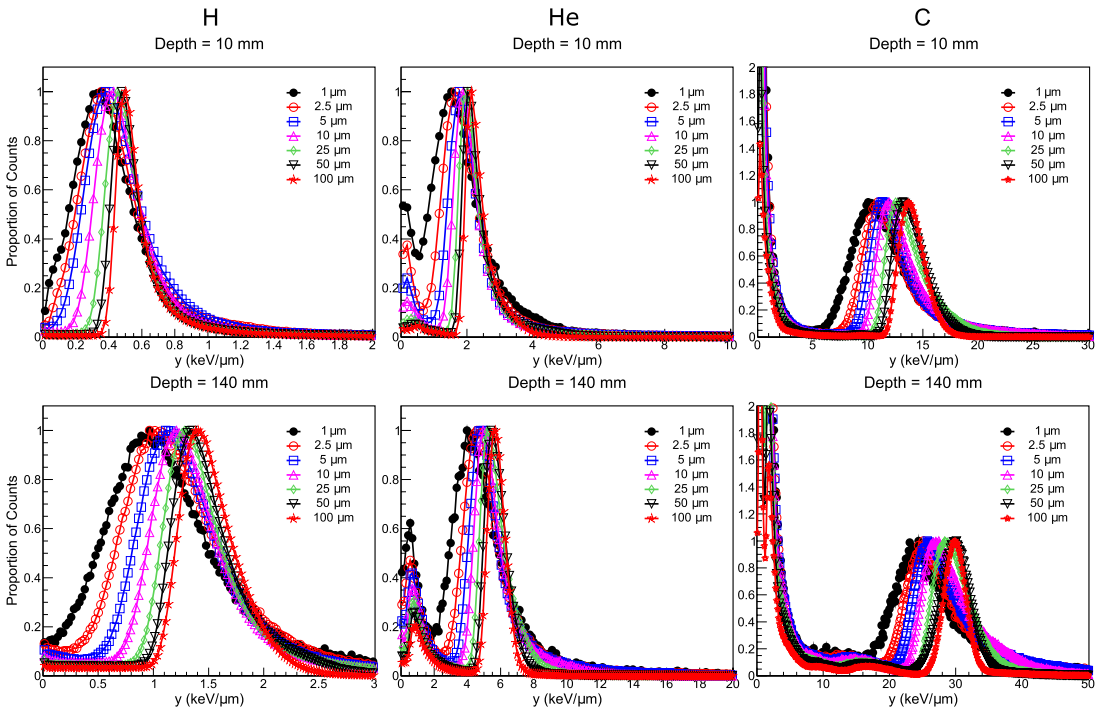

Figure 3. Comparison of the lineal energy spectra of different sized SVs in the different mono-energetic beams at a depth of 10 mm (top plots) and at 140 mm (bottom plots).

are plotted on a linear scale instead of the more traditional semi-log scale. This is done to preserve the detail of the curves which may be diminished after rebining when multiple bins are placed into a single bin, potentially causing averaging effects. The left most peak in the spectra (below ~1 keV μm^{-1}), which is most readily seen for the ^{4}He and ^{12}C ion beams, is due to electrons which are produced outside of the SV. The electron peak is not readily observed in the proton spectra at most depths due to the lineal energy of the electrons and protons having similar values, except near the BP. Even near the BP, the electron peak is still much less prominent than the heavier beams due to its much smaller production of electrons. The smaller peaks between the electron and the primary beam peak, which are seen in the ^{12}C ion spectra, are due to different types of fragments.

The peak position of the distributions are seen to shift to higher lineal energies when the SV size increases, with the peak of the distribution becoming sharper for larger SVs. Figure 4 plots the peak position and the FWHM of the peak of the lineal energy spectra shown in figure 3 as well as other depths up to 160 mm. In the case of the ^{4}He and ^{12}C beams, the peak refers to the right peak in the spectra due to the primary ion beam. The peak positions and widths values are from the fitted three term Gaussian distributions.

The proportion which the width of the proton peak decreases with thicker SVs does not vary significantly at different depths, with the width from a 1 μm thick SV decreasing by ~15% when increasing the thickness to 10 μm and decreasing by ~55% when increasing to 100 μm thick (with respect to the 1 μm thick SV).

For ^{4}He ion beams the width of the peak is more sensitive to SV thickness, with the peak decreasing by ~40% when increasing the thickness to 10 μm. When the thickness of the SV increases to 100 μm from 1 μm the peak width decreases by ~60%, which is more similar to what was seen for the proton beam. For ^{12}C the peak width decreases slightly less than the ^{4}He beam with a reduction of ~30% and ~40% when comparing the 1 μm thick SV to the 10 and 100 μm thick SVs, respectively.

The more traditional representation of the microdosimetric spectra, using the dose weighted distribution $d(y) = yf(y)/\overline{y_F}$, is shown in figure 5 at a depth of 10 mm, the scale of the y-axis is in $yd(y)$ due to the linear spaced bins being re-binned into log bins (ICRU Report 36-Microdosimetry 1983, Bradley *et al* 2001). Instead of representing just the distribution of lineal energy events in the SV, $d(y) = (yf(y)/y_F)$ weights the distribution to higher lineal energies to represent their contribution to the dose. Once the distribution is weighted the impact of straggling is more easily seen, with the smaller SVs extending to much higher values. For the proton beam the 1 μm thick SV is seen to have a tail which extends to ~100 keV μm^{-1} while the 10 and 100 μm thick SVs fall sharply at ~10 and ~1 keV μm^{-1}, respectively.

From the thinnest SV thickness of 1 μm to the thickest one of 100 μm, all beams' lineal energy spectra are seen to have their peak shift to higher lineal energies and narrower distributions. The fluctuations of energy lost in a medium by a charged particle are dependent on the number of ionisations and excitations which occur and how much energy is transferred in each of these collisions. The number of ionisations/excitations follow a

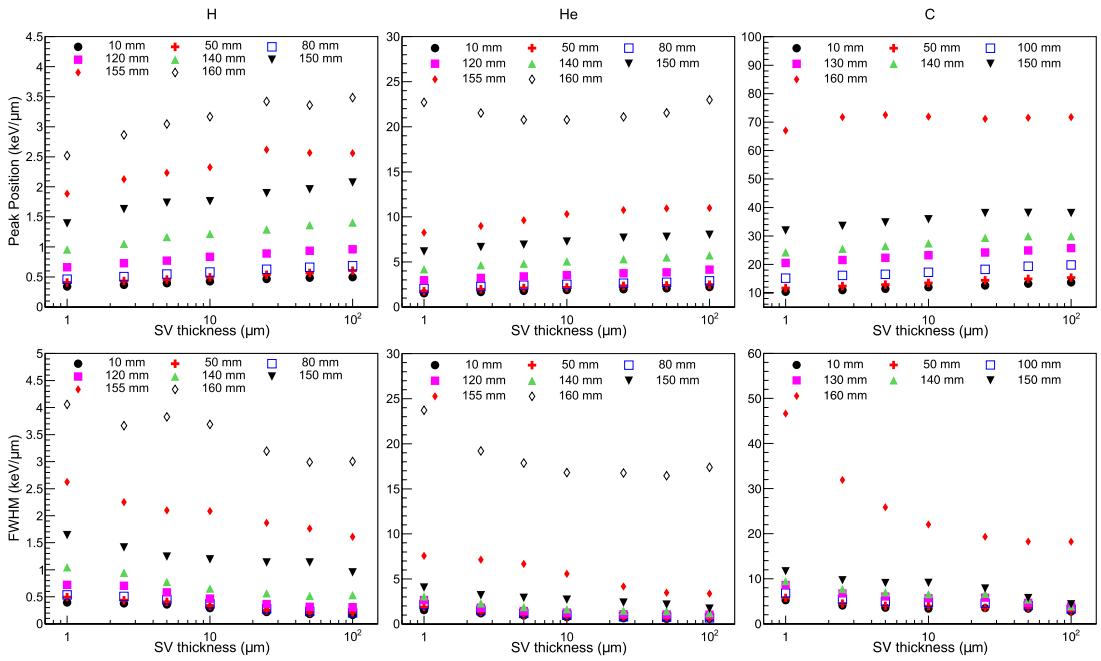

Figure 4. Comparison of the peak position (top) and the FWHM (bottom) of the lineal energy spectra which was fitted using a three term Gaussian function.

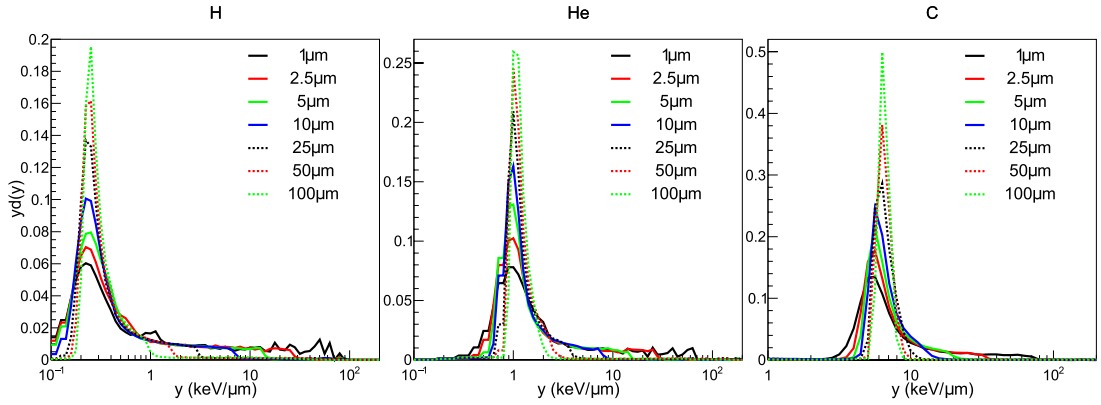

Figure 5. Comparison of the $yd(y)$ spectra (which is equivalent to the $d(y)$ distribution when plotted with linearly spaced bins) for the different sized SVs when irradiated in the three mono-energetic beams at a depth of 10 mm.

Poisson distribution while the energy transferred in these events depend on single collision spectra for the projectile and medium (Rossi and Zaider 1996). The number of ionisations and excitations in a medium are proportional to Z^2/v^2, where Z is the charge of the projectile and v is its velocity. The single collision spectra follows a more complex distribution, with many theoretical descriptions formulated to describe experimental distribution such as Landau-Vavilov (Landau 1944). Except for extreme relativistic energies, the maximum energy transferred to an electron is proportional to the projectile's velocity squared, for the same kinetic energy a proton will have a greater velocity than heavier ions. The calculated lineal energy spectra of smaller SVs can be seen to have more prominent tails which extend to higher energies compared to larger SVs. Due to fewer ionisations occurring it is more likely to have a larger portion of these ionisations transfer energies to the electrons which is closer to the maximum possible energy.

3.2. Impact on $\overline{y_F}$

The $\overline{y_F}$ depth distributions for the three mono-energetic beams are shown in figure 6, the vertical dashed line corresponds to the position of the pinnacle of the BP. The percentage difference, PD, is plotted on the bottom of the curves with respect to the 10 μm thick SV. For the proton and ^{4}He beams there is very little difference between the different SVs, while the ^{12}C beam shows a considerable difference. For all beams the larger SVs are seen to have the largest $\overline{y_F}$. The proton beams have a maximum difference of $\sim$2% at the entrance of the phantom, which gradually decreases with increasing depth. The ^{12}C beam has a difference of $\sim$40% between the case of 10 μm

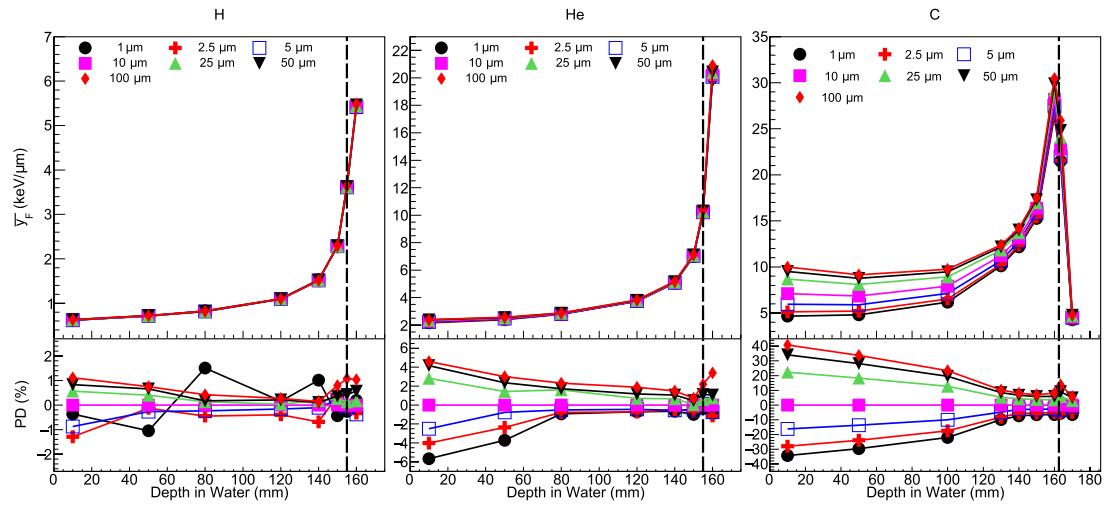

Figure 6. Comparison of the mean lineal energy, $\overline{y_F}$, for a mono-energetic 150 MeV proton beam (left), 150 MeV/u ^{4}He beam (middle) and a 290 MeV/u ^{12}C ion beam (right).

and the 100 μm thick SV, with the 1 μm having a value $\sim$40% lower at the surface of the phantom and decreasing to $\sim\pm$10% at 130 mm.

3.3. Impact on $\overline{y_D}$

The $\overline{y_D}$ distributions along the Bragg curves of the mono-energetic beams are shown in figure 7 for the different thicknesses of SVs. The $\overline{y_D}$ results differ quite drastically from the $\overline{y_F}$ distributions, with the proton beams having the largest variation while the ^{12}C beam shows the least impact from SV size. In the case of the proton beam the 1 μm thick SV has a value $\sim$200% higher than the 10 μm thick SV with the difference decreasing after 120 mm in water. The difference of $\overline{y_D}$ quickly drops as the SV size increases. When comparing the ^{12}C beam the 1 μm thick SV has the largest difference with a value of $\sim$30% while all other SVs have differences within $\sim$10%.

Additionally, the shape of the proton distributions of the 1 and 2.5 μm can be seen to differ quite drastically compared to the other sizes of volumes and beam types, with a large value at the start which decreases towards the BP and increases again. The cause of this high $\overline{y_D}$ value can be seen in figure 5, where the lineal energy spectra extends to larger values compared to the thicker SVs. As such, this makes $\overline{y_D}$ measurements quite sensitive to the maximum lineal energy being detected and is illustrated in figure 8. Figure 8 shows the $\overline{y_D}$ distributions for the 1 μm thick volume but with different maximum lineal energies, as indicated by the legend.

3.4. Impact on RBE

The calculated RBE profiles, as estimated using the MKM, along the depth of the different mono-energetic beams are shown in figure 9. RBE was calculated using equation (10) for protons and for heavier beams equation (9) was used. The obtained profiles follow a similar trend as $\overline{y_D}$, with the proton beam again having the largest impact from SV size, with the smaller sizes having larger values of RBE. For proton beams, the difference between the largest and smallest SV is $\sim$30% while for ^{4}He and ^{12}C have a similar value of $\sim$10%. The impact of the SV size on the RBE estimation, despite following the same trend, is reduced compared to $\overline{y_D}$. The RBE is less sensitive due to the $y*$ quantity which is similar to $d(y)$ but reduces the dominance of higher y events. Additionally, RBE is calculated with various cell specific constants which reduces the effect of the lineal energy spectra.

3.5. Contribution of particles to quantities

To see the effect which the primary beam and delta electrons has on the different microdosimetric quantities, the events (energy deposition of a particle as it traverses the SV) in the SV can be processed in two different ways. The first way is to filter all events which are only from the incident primary beam (including electrons it generates in the SV) and the second is to filter all events except electrons which enter the SV (not generated within the SV). Figures 10 and 11 show $\overline{y_F}$, $\overline{y_D}$ and RBE when considering only electrons which enter the SV (top) and the incident primary beam (bottom) for proton and ^{12}C beams, respectively.

Comparing the $\overline{y_F}$ values when processing only electrons which enter the SV, the difference is similar for all three beams (only proton and ^{12}C ion beams shown). When processing only electron events the $\overline{y_F}$ of proton and ^{4}He beams have a slight less variation on size than the ^{12}C beam, with a difference of $\sim$20% at the surface of the phantom while the difference for an incident ^{12}C ion beam is $\sim$30%. This difference is due to the different energy spectra of delta electrons generated by the beams, with ^{12}C ions having a maximum energy approximately

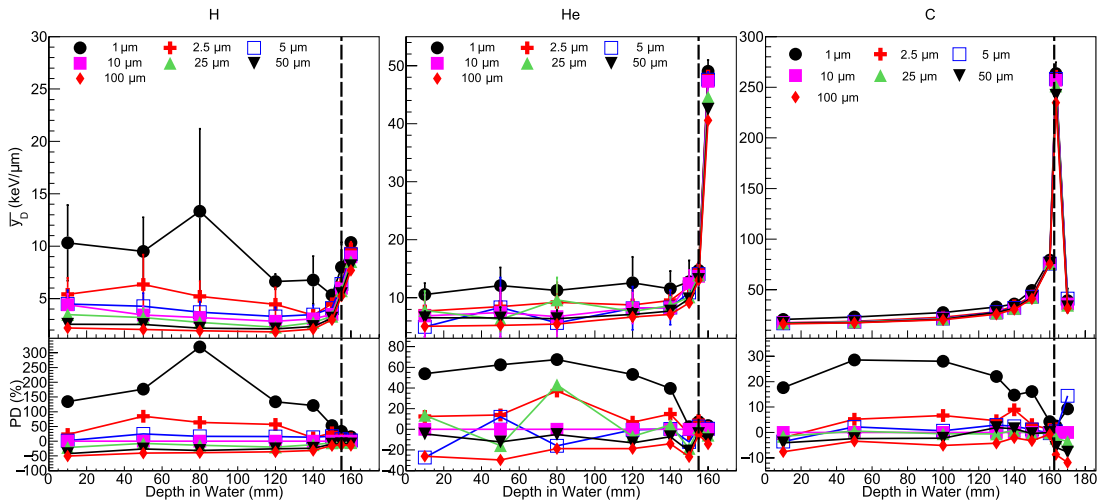

Figure 7. Comparison of the dose mean lineal energy, $\overline{y_D}$, for a mono-energetic 150 MeV proton beam (left), 150 MeV/u ^{4}He beam (middle) and a 290 MeV/u ^{12}C ion beam (right).

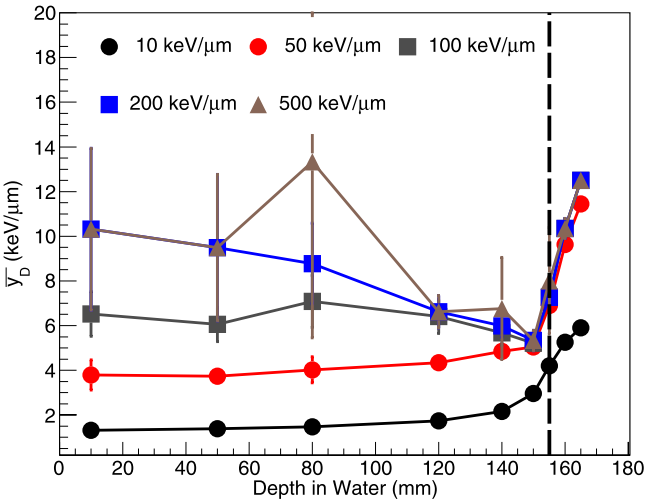

Figure 8. The effect of different maximum lineal energies on the dose mean lineal energy, $\overline{y_D}$, for the 1 μm thick design when placed in a mono-energetic 150 MeV proton beam.

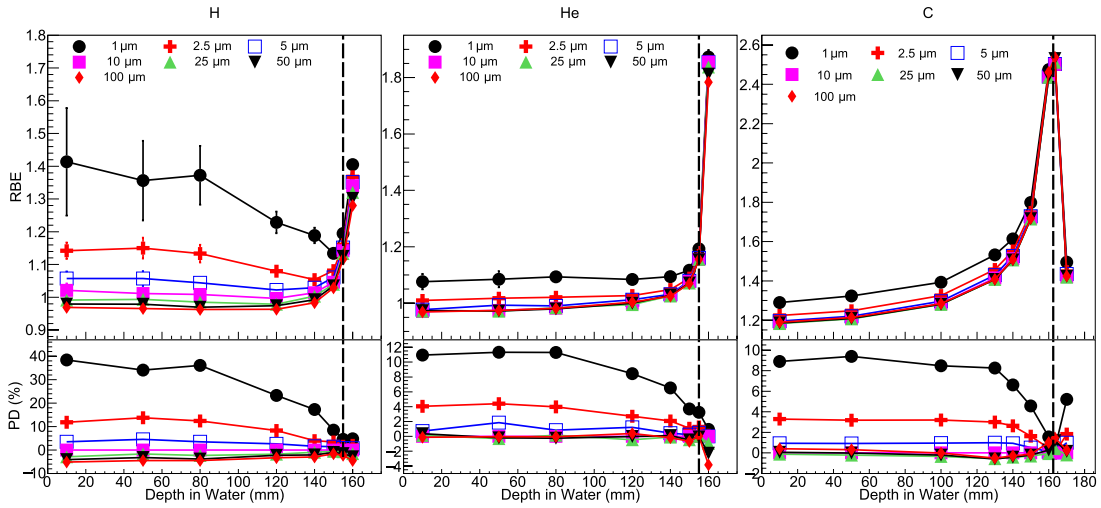

Figure 9. Comparison of the RBE for a mono-energetic 150 MeV proton beam (left), 150 MeV/u ^{4}He beam (middle) and a 290 MeV/u ^{12}C ion beam (right).

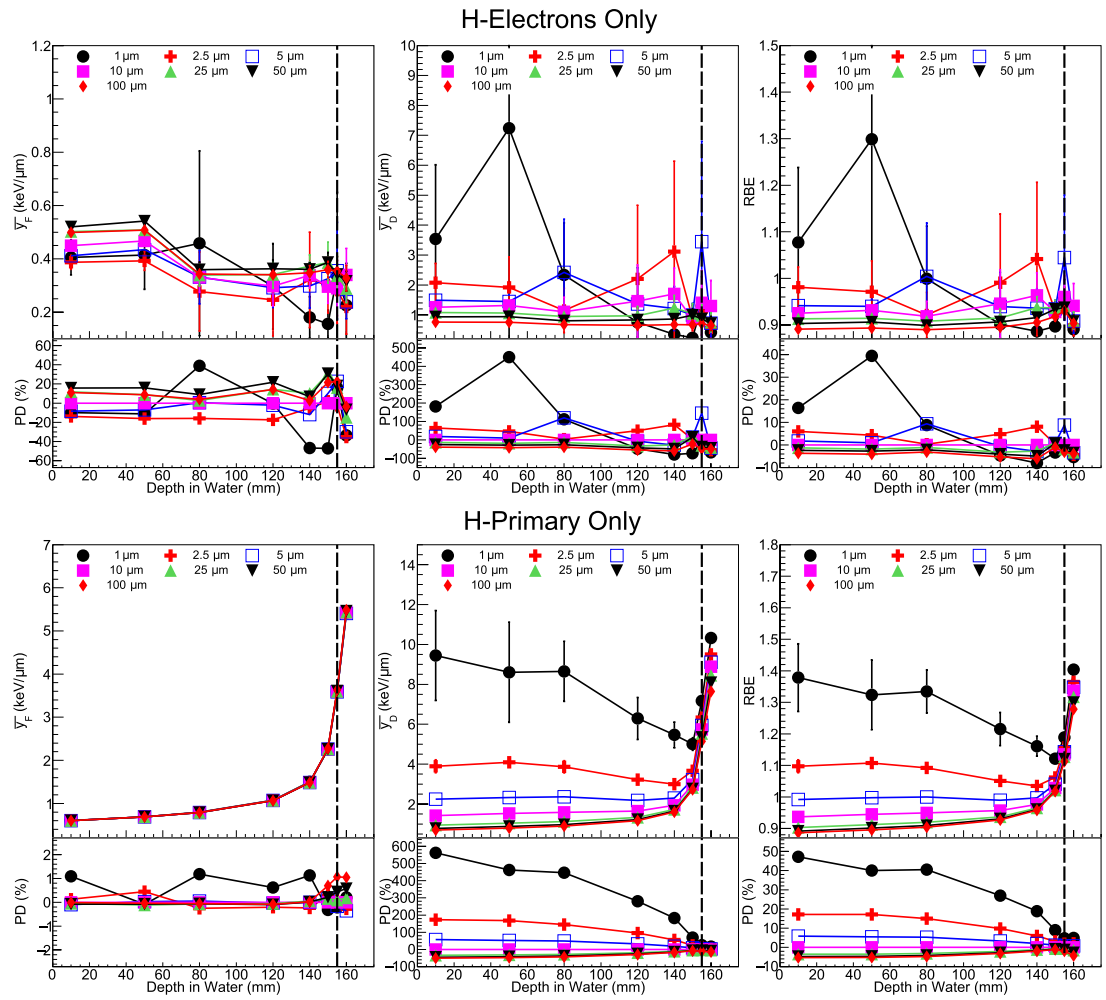

Figure 10. A comparison of the PD of different SV thicknesses in a mono-energetic proton beam when only electrons which are generated outside of the SV and enter are considered (top) as well as the incident primary beam (bottom).

twice the proton/^{4}He beams. This higher energy of delta electrons causes $\overline{y_F}$ to be more sensitive to the size of the SV due to the proportion of electrons stopping in detector changing more along the depth of the phantom. This can be seen for ^{12}C after ~100 mm depth, the $\overline{y_F}$ has a similar range of values as proton does at 10 mm. After 100 mm the maximum energy of the ^{12}C ion delta electrons has halved from its values at 10 mm (~0.7 MeV) and corresponds to the same maximum delta electron energy of protons at 10 mm (~0.35 MeV). ^{12}C ions produce many more delta electrons than ^{4}He ions and even more than protons. This difference in the electron production causes y_F measurements in larger ion beams to be more sensitive to the SV size than for smaller ions. For ^{4}He and ^{12}C the difference in $\overline{y_F}$ for different SV sizes was seen to decrease with increased depth.

Comparing the different quantities when only the incident beam is considered (bottom plots of figures 10 and 11), both beams do not have their y_F vary with SV thickness while $\overline{y_D}$ is strongly dependent. This shows that the observed variation in $\overline{y_F}$ seen in figure 6 is due to electrons in the radiation field, with ^{12}C being more sensitive to the SV size due to the greater production of delta electrons. The difference in y_F when processing just primary beam events is not affected because the mean of the lineal energy is effectively representing the linear energy transfer of the incident ion, which will not vary based on the SV thickness except at very low energies where the stopping power changes rapidly. Due to the additional y dependency of y_D, the spectrum is weighted to higher energy deposition events.

The RBE results showed a similar trend as $\overline{y_D}$, but with a reduced difference due to the smaller impact of higher y events. The SV thicknesses between 5 and 100 μm, which are equivalent to muscle thicknesses of ~8.5–175 μm, show only slight differences of ~1%.

The difference between the quantities of $\overline{y_F}$, $\overline{y_D}$ and RBE for different thicknesses are all seen to reduce with depth. For $\overline{y_F}$ this is due to the lower energy of delta electrons produced and causing the majority of electrons to stop in the SV, regardless of the thickness . The differences due to the SV thickness of $\overline{y_D}$ and RBE are instead dependent on the primary beam, as the energy of the beam decreases with depth the number of ionisations/excitations in the medium increases, creating a sharper distribution.

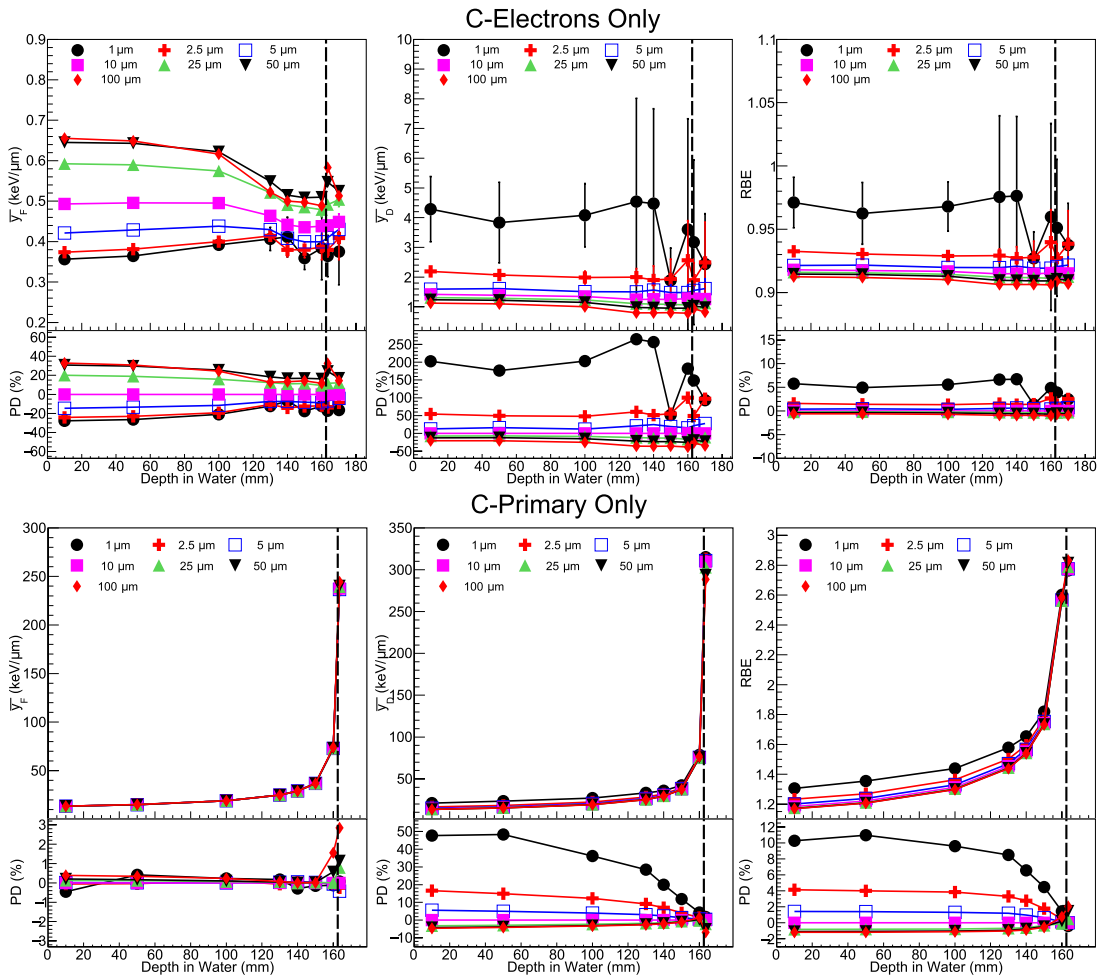

Figure 11. A comparison of the PD of different SV thicknesses in a mono-energetic ^{12}C ion beam when only electrons which are generated outside of the SV and enter are considered (top) as well as the incident primary beam (bottom).

3.6. Comparison with spherical SVs

Figure 12 shows the distributions of the three different quantities of interest when the cylindrical SVs are replaced with spheres. The percentage difference values are calculated with respect to the 15 μm diameter sphere, which corresponds to a mean chord length of 10 μm. Unsurprisingly, the sphere volumes which give the best agreement with the cylinder volumes are those with a mean-chord length equal to the thickness of the cylinder. With the 1.5 μm diameter sphere giving the best agreement with the 1 μm thick cylinder sensitive volume. For the case of the proton beam, there is no significant difference in the quantities between the corresponding sizes of cylinders and spheres. The ^{12}C ion beam however results in differences of $\sim$3% between the cylinders and spheres for all three quantities. Since there is only a significant difference for the ^{12}C ion beam and not the proton beam, the cause of this difference may be due to the denser electron track structure of the ^{12}C ion. It was observed that the ratio of the distance which an electron travelled in a volume compared to the primary particle was slightly higher for spheres than cylinders, which would cause a slight increase in the lineal energy, when calculating the lineal energy using the mean path length of the primary beam.

4. Discussion

As mentioned in the introduction, the majority of human cell nuclei have diameters between $\sim$2–10 μm, corresponding to $\sim$1–5 μm of silicon. Ideally, measuring the lineal energy spectrum of a beam with SVs throughout this range of sizes would result in similar distributions and quantities, such as $\overline{y_D}$. Or even more ideally, if a thicker SV on the order of $\sim$100 μm could be used with minimal change in spectra and quantities since these thicknesses are close to 'off-the-shelf' devices such as Hamamatsu silicon photodiodes with active areas between $\sim$1–100 mm^2 (Hamamatsu 2019). However, to avoid pile-up of the detector read-out system (Usman and Patil 2018), which commonly occur for count rates of over $\sim$2000 per second in the detector, the dose rates of beams must be smaller for larger single SV detectors compared to much smaller dedicated microdosimeter designs. Current generation SOI devices include options for total active areas of $\sim$900 μm^2, allowing them to be

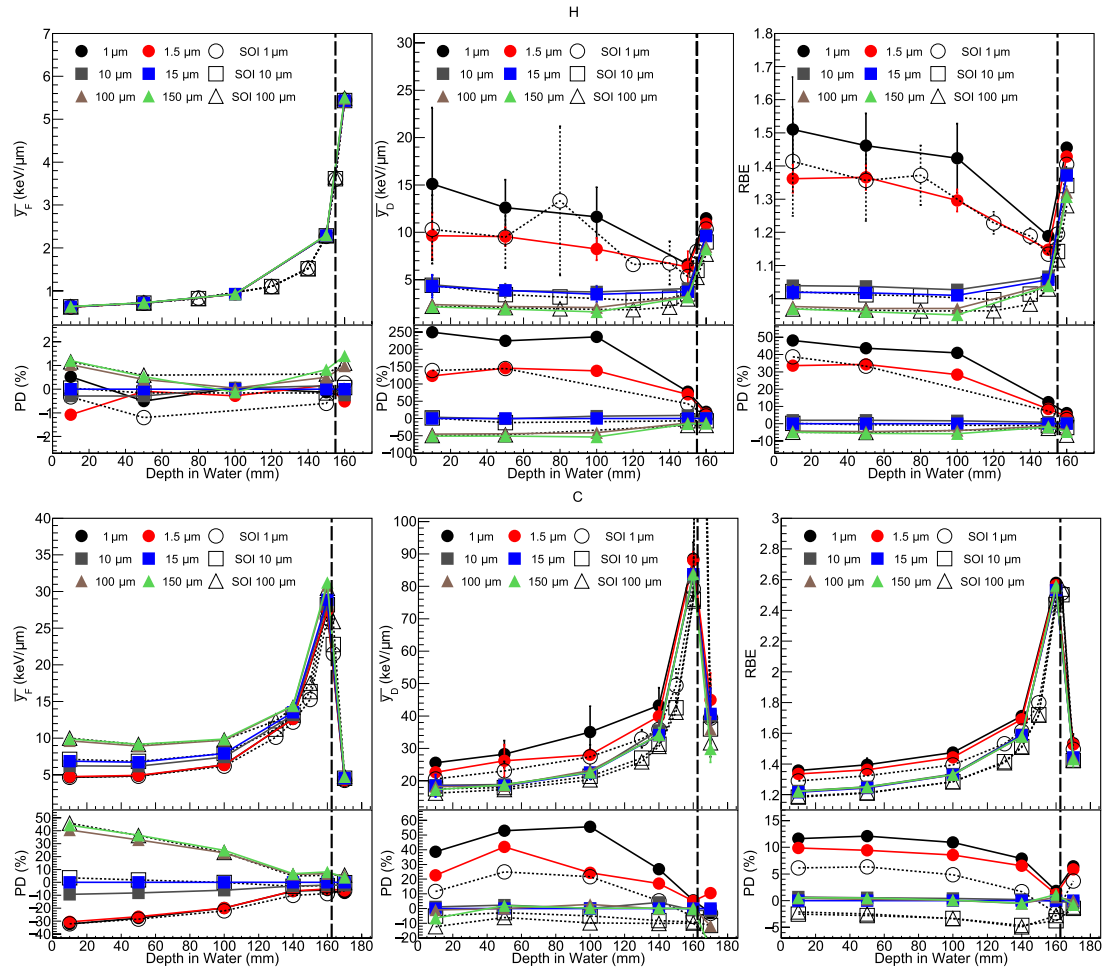

Figure 12. Comparison of the different quantities of interest when replacing the cylinder SVs of the microdosimeter with spheres. The top graphs show the results for the proton beam while the bottom plots show the results for the ^{12}C ion beam. The thickness/diameter of the spheres are displayed in the legend, with the middle column of the legend (1.5, 15, 150 μm) corresponding to a mean chord length equal to the thickness of the cylinders (right column).

operated in therapeutic dose rates, which for proton and ^{12}C ion therapy are typically $\sim 10^{12}$ (Jones *et al* 2016) and $\sim 10^{9}$ (Kitagawa *et al* 2010) particles a second, respectively. Additionally, a single large SV, in proton therapy especially, causes a large variation in the path length of charged particles in the SV along the Bragg curve (Bolst *et al* 2018). These factors would restrict the possible use of off-the-shelf solutions to low dose rate beams of heavy ions.

Unfortunately, for SV thicknesses between the range of 1–5 μm, showed the greatest sensitivity to the microdosimetric spectra and values of $\overline{y_F}$, $\overline{y_D}$ and RBE. With the SV thickness affecting $\overline{y_F}$ significantly for heavier ion beams and $\overline{y_D}$ for lighter beams. Focusing on the RBE of ^{12}C ions, which is clinically of the most interest out of the three quantities and beams compared, showed maximum differences of $\sim 8\%$ between the 1 and 5 μm thick volumes at the entrance of the BP. Though at the end of the primary beam's range all SV thicknesses converge to the same value of RBE. However, when creating a treatment plan for a patient it is planned based on the biological dose, which is the product of the RBE and physical dose for a particular position. If you consider a mono-energetic ^{12}C ion beam with an initial energy of 290 MeV/u, the ratio of the maximum dose at the pinnacle of the BP to the entrance dose is approximately 4–1. Since all SV thicknesses converge to the same value of RBE at the pinnacle of the BP, where the RBE is maximum for a ^{12}C ion, if the biological dose is calculated at the BP, with the entrance dose normalised to 1, all SV thicknesses give a biological dose of 10 if the maximum value calculated in this work is used (though the true maximum RBE of a mono-energetic 290 MeV/u ^{12}C ion is closer to 3, but this point was not simulated). Similarly, if the biological dose at the entrance is calculated using the thinnest and thickest SV values the of RBE biological dose is 1.29 and 1.19, respectively. So in terms of the biological dose the significance of the SV thickness is reduced. One additional positive aspect observed for this configuration is that the difference in the RBE is constant for all the SVs before the dose begins building at the BP region, which would allow for scaling of values at the surface, generally where healthy tissue is located.

Since it is desirable to avoid having to apply corrections, so for maximum flexibility and accuracy, an appealing design for future SOI designs would be to incorporate multiple thicknesses between ∼1–10 μm (tissue equivalent) and allow for each thickness of SV to be read out separately. This would allow multiple types of cell nuclei to be represented and to have their lineal energy distributions measured simultaneously.

5. Conclusions

The impact of the SV thickness of SOI microdosimeters was investigated in therapeutic mono-energetic proton, ^{4}He and ^{12}C ion beams. SV thicknesses were investigated between 1 and 100 μm. Larger SV thicknesses were seen to cause the lineal energy spectra peak to be shifted to higher energies and produce a sharper peak.

The microdosimetric quantity, y_F was seen to be strongly influenced by the different electron track densities of the beams. ^{12}C had the greatest impact from the SV size due to the much higher delta electron production, with a difference of ∼40% between the 1 and 10 μm thick SVs, while the proton beam only had a maximum difference of ∼2% and ^{4}He ∼6%.

In contrast to $\overline{y_F}$, $\overline{y_D}$ was dependent on the incident primary beam, with protons being the most sensitive to different thicknesses of SV due to it having the largest possible energy transfer to electrons for a given energy. The difference between 1 and 10 μm thick SVs was ∼250%, ∼120% and ∼30% at the surface of the phantom for the proton, ^{4}He and ^{12}C beams, respectively. The calculated RBE, estimated by the MKM, had a similar dependence as $\overline{y_D}$ but with a reduced percentage difference due to higher lineal energy events having less effect. The difference at the surface between the 1 and 10 μm thick SVs was ∼30%, 11% and 9% for the proton, ^{4}He and ^{12}C beams, respectively.

Since $\overline{y_F}$ is generally of less interest for clinical applications than $\overline{y_D}$, the SV size when used in proton beams should be carefully considered when comparing different measurements due to the large dependency on the SV thickness/size. Conversely, when comparing biological estimation measurements for heavy ion beams, comparisons are less sensitive to the size of the SV.

Acknowledgment

This work was supported by computational resources provided by the Australian Government through the Raijin cluster under the National Computational Merit Allocation Scheme.

ORCID iDs

D Bolst https://orcid.org/0000-0002-0257-1267
S Guatelli https://orcid.org/0000-0002-9289-7956

References

Agostinelli S *et al* 2003 Geant4-a simulation toolkit *Nucl. Instrum. Methods Phys. Res.* A **506** 250–303
Allison J *et al* 2006 Geant4 developments and applications *IEEE Trans. Nucl. Sci.* **53** 270–8
Allison J *et al* 2016 Recent developments in Geant4 *Nucl. Instrum. Methods Phys. Res.* A **835** 186–225
Arce P *et al* 2020 Report on G4-Med, a Geant4 benchmarking system for medical physics applications developed by the Geant4 medical physics benchmarking group *Med. Phys.* accepted
Bolst D *et al* 2017a Validation of Geant4 fragmentation for heavy ion therapy *Nucl. Instrum. Methods Phys. Res.* A **869** 68–75
Bolst D, Guatelli S, Tran L and Rosenfeld A 2018 Optimisation of the design of SOI microdosimeters for hadron therapy quality assurance *Phys. Med. Biol.* **63** 215007
Bolst D, Guatelli S, Tran L, Chartier L, Lerch M, Matsufuji N and Rosenfeld A 2017b Correction factors to convert microdosimetry measurements in silicon to tissue in ^{12}C ion therapy *Phys. Med. Biol.* **62** 2055
Bolst D *et al* 2019 Validation of Geant4 for silicon microdosimetry in heavy ion therapy *Phys. Med. Biol.* (https://doi.org/10.1088/1361-6560/ab586a)
Bradley P D and Rosenfeld A B 1998 Tissue equivalence correction for silicon microdosimetry detectors in boron neutron capture therapy *Med. Phys.* **25** 2220–5
Bradley P D, Rosenfeld A B and Zaider M 2001 Solid state microdosimetry *Nucl. Instrum. Methods Phys. Res.* B **184** 135–57
Chartier L *et al* 2017 Microdosimetric applications in proton and heavy ion therapy using silicon microdosimeters *Radiation Protection Dosimetry* pp 1–7 (https://doi.org/10.1093/rpd/ncx226)
De Nardo L, Cesari V, Don G, Magrin G, Colautti P, Conte V and Tornielli G 2004 Mini-TEPCs for radiation therapy *Radiat. Prot. Dosim.* **108** 345–52
Debrot E *et al* 2018 SOI microdosimetry and modified MKM for evaluation of relative biological effectiveness for a passive proton therapy radiation field *Phys. Med. Biol.* **63** 235007
Far West Technology, Inc 2001 *Model LET-1/2 Operation Manual*
Hamamatsu 2019 *Si photodiodes Product Catalogue* www.hamamatsu.com/jp/en/product/optical-sensors/photodiodes/si-photodiodes/index.html

Hawkins R B 1994 A statistical theory of cell killing by radiation of varying linear energy transfer *Radiat. Res.* **140** 366–74
ICRU Report 36-Microdosimetry 1983 (Bethesda, MD: International Commission on Radiation Units and Measurements)
ICRU Report 78-Prescribing, Recording and Reporting Proton-Beam Therapy 2007 *Report* (Bethesda, MD: International Commission on Radiation Units and Measurements)
Jones B and Dale R G 2000 Estimation of optimum dose per fraction for high let radiations: implications for proton radiotherapy *Int. J. Radiat. Oncol. Biol. Phys.* **48** 1549–57
Jones K C, Seghal C M and Avery S 2016 How proton pulse characteristics influence protoacoustic determination of proton-beam range: simulation studies *Phys. Med. Biol.* **61** 2213–42
Jones L, Hoban P and Metcalfe P 2001 The use of the linear quadratic model in radiotherapy: a review *Australas. Phys. Eng. Sci. Med.* **24** 132–46
Kase Y, Kannai T, Matsumotot Y, Furusawa Y, Okamato H, Asaba T, Sakama M and Shinoda H 2006 Mirodosimetric measurements and estimation of human cell survival for heavy-ion beams *Radiat. Res. Soc.* **166** 629–38
Kase Y, Yamashita W, Matsufuji N, Takada K, Sakae T, Furusawa Y, Yamashita H and Murayama S 2013 Microdosimetric calculation of relative biological effectiveness for design of therapeutic proton beams *J. Radiat. Res.* **54** 485
Kellerer A M 1984 Chord length distributions and related quantities for spheroids *Radiat. Res.* **98** 425–37
Kellerer A M 1985 2-fundamentals of microdosimetry *The Dosimetry of Ionizing Radiation* ed K R Kase *et al* (New York: Academic) pp 77–162
Kitagawa A, Fujita T, Muramatsu M, Biri S and Drentje A 2010 Review on heavy ion radiotherapy facilities and related ion sources *Rev. Sci. Instrum.* **81** 02B909
Kliauga P 1990 Measurement of single event energy deposition spectra at 5 nm–250 nm simulated site sizes *Radiat. Prot. Dosim.* **31** 119–23
Landau L D 1944 On the energy loss of fast particles by ionization *J. Physique* **8** 201–5
Masters J R 2002 Hela cells 50 years on: the good, the bad and the ugly *Nat. Rev. Cancer* **2** 289–320
Maul G and Deaven L 1977 Quantitative determination of nuclear pore complexes in cycling cells with differing dna content *J. Cell Biol.* **73** 748–60
Milo R and Phillips R 2015 *Cell Biology by the Numbers* (London: Taylor & Francis)
Nikjoo H, Emfietzoglou D, Liamsuwan T, Taleei R, Liljequist D and Uehara S 2016 Radiation track, dna damage and responsea review *Rep. Prog. Phys.* **79** 116601
Rosenfeld A B 2016 Novel detectors for silicon based microdosimetry, their concepts and applications *Nucl. Instrum. Methods Phys. Res.* A **809** 156–70 (Advances in detectors and applications for medicine)
Rossi H H 1970 The effects of small doses of ionizing radiation *Phys. Med. Biol.* **15** 255
Rossi H H and Zaider M 1996 *Microdosimetry and Its Applications* (Berlin: Springer)
Schardt D, Elsässer T and Schulz-Ertner D 2010 Heavy-ion tumor therapy: physical and radiobiological benefits *Rev. Mod. Phys.* **82** 383–425
Selva A, Conte V, Colautti P, Chiriotti S, Fazzi A, Pola A, Bortot D, Agosteo S and Ciocca M 2017 Microdosimetric study at the CNAO active-scanning carbon-ion beam *Radiat. Prot. Dosim.* **180** 157–61
Tran L T *et al* 2018 The relative biological effectiveness for carbon, nitrogen, and oxygen ion beams using passive and scanning techniques evaluated with fully 3D silicon microdosimeters *Med. Phys.* **45** 2299–308
Tran L T *et al* 2017 Characterization of proton pencil beam scanning and passive beam using a high spatial resolution solid state microsimeter *Med. Phys.* **44** 6085–95
Usman S and Patil A 2018 Radiation detector deadtime and pile up: a review of the status of science *Nucl. Eng. Technol.* **50** 1006–1016